Diffusion and structural changes in $Fe_{91-y}Mo_8Cu_1B_y$ alloys

2007 J. Phys.: Condens. Matter 19 156219

(http://iopscience.iop.org/0953-8984/19/15/156219)

IOP PUBLISHING JOURNAL OF PHYSICS: CONDENSED MATTER

J. Phys.: Condens. Matter **19** (2007) 156219 (16pp) doi:10.1088/0953-8984/19/15/156219

Diffusion and structural changes in $Fe_{91-y}Mo_8Cu_1B_y$ alloys

J Čermák and I Stloukal

Institute of Physics of Materials, AS CR, Žižkova 22, CZ-61662 Brno, Czech Republic

E-mail: cermak@ipm.cz and stloukal@ipm.cz

Received 9 November 2006, in final form 16 January 2007
Published 26 March 2007
Online at stacks.iop.org/JPhysCM/19/156219

Abstract

Fe and Mo tracer diffusion in $Fe_{91-y}Mo_8Cu_1B_y$ alloys was studied by the serial sectioning method in the temperature interval 548–773 K. The measurement was done with three alloys differing in Fe/B ratio ($y = 12$, 15 and 17) prepared by the planar flow casting technique, in relaxed and crystallized states. Three modes of Fe diffusion were observed: (i) the slowest one is volume diffusion in the relaxed amorphous (RA) phase, (ii) faster diffusion occurs along the interfaces between crystallites (C) and the RA phase, and (iii) the fastest diffusion was observed along grain boundaries (C/C). It was found that the rate of Mo volume diffusion in the relaxed amorphous phase is approximately the same as that of Fe, but Mo diffusion is much slower than Fe diffusion in grain boundaries. The activation enthalpy of Mo grain boundary diffusion increases with increasing concentration of B. The characteristics of short-circuit diffusion in structures where the relative fraction of RA/C-type interfaces prevail over the C/C-type ones depend sensitively on the thermal treatment.

1. Introduction

Magnetically soft nanocrystalline materials (NMs) prepared by very rapid quenching of the melt and by subsequent annealing the solid have been at the focus of interest for the last 15 years [1]. As regards the chemical composition, they form a broad family of materials reviewed, for example, in [2]. They consist of a ferromagnetic element (or some combination), of a large-atom element (so-called *early transition* element from groups 4–6), of a metalloid or semi-metal, and of a *late transition* element (group 11) whose mixing enthalpy with the ferromagnetic element is positive.

Excellent soft magnetic characteristics of NMs follow from their microstructure. The main advantage of these materials is very high effective permeability ($\mu_e \sim 10^5$), high saturation magnetization ($M_s \sim 1.7$ T) and low coercivity ($H_c \leqslant 1$ A m^{-1}). The link between the

microstructure and magnetic parameters follows, above all, from the fact that the typical size of fine crystallites is comparable to the typical length of atomic exchange interaction.

Since NMs are applied in a thermodynamically unstable state, it is clear that knowledge of the diffusion characteristics that quantify the rate of structural changes—and, at the same time, the magnetic behaviour of the materials—is of primary importance. It follows, however, from the merits of the case that the tracer diffusion measurements must be carried out very carefully at sufficiently low temperatures and for short diffusion times in order to keep the structure unchanged during the experiment (for a review of specific features of the diffusion experiments with NMs, see, for example, in [3]). This can, of course, be fulfilled only approximately.

Hence, the fine sectioning of a thin diffusion zone by Ar^+-ion sputtering [4] is applied in order to obtain the diffusion data at low temperatures. However, the reconstruction of the true concentration profile obtained by sputtering is not an easy task due to mixing-roughness-information (MRI) depth [5]. By fine depth profiling of thin layers, with thicknesses of about one to ten nanometres, the deconvolution method of data evaluation should be applied.

It is a matter of fact that the obtained profiles are frequently scattered and curved, which makes their interpretation difficult (see, e.g., [6]). Nevertheless, there are measurements in the literature that allow us to distinguish between the diffusion mechanisms on the basis of the shape of the penetration profile [7].

In the present paper, careful diffusion measurement of Fe and Mo diffusion coefficients in $Fe_{91-y}Mo_8Cu_1B_y$ ($y = 12, 15, 17$) alloys is carried out over the diffusion zone, whose thickness is much greater than the MRI depth. An attempt is made to assign the diffusion coefficients to diffusion in specific structural components of the alloys studied.

Molybdenum, as an *early transition element*, is a metal that has not been used frequently in NMs up to now. However, it results in very low Curie temperatures ($T_C \sim$ room temperature) both in the quenched state and in relaxed and partly crystallized states of the alloy, which promises interesting applications in the future. The magnetic properties of the system were reported in [8–11], influence of the Fe/B ratio on the thermodynamic properties was studied in [12] and the kinetic characterization of nanocrystal formation in $Fe_{76}Mo_8Cu_1B_{15}$ was done in [13]. It was found [13] that the devitrification of FeMoCuB is a multistage process that does not follow the simple Johnson–Mehl–Avrami kinetics. Therefore, knowledge of the diffusion characteristics of the principal constituents in FeMoCuB alloys may contribute to better understanding the crystallization behaviour of this type of alloy.

2. Experimental details

2.1. Preparation of alloys and thermal treatment

Three experimental alloys, $Fe_{91-y}Mo_8Cu_1B_y$, differing in Fe/B ratio (see table 1) were prepared in the Department of Metal Physics, Institute of Physics SAS, Slovakia by a planar flow casting technique as ribbons of about 10 mm width and about 30 μm thickness.

Circular diffusion samples (diameter 10 mm) were die cut from the ribbons with a presser and—prior to diffusion experiments—subjected to five different thermal treatments, described in table 2.

The relaxation temperature of $t3$, $t4$, $T_r = 773$ K, was chosen to be close to the temperature of primary crystallization, T_{cr} ($T_r \approx T_{cr}$ for the alloy B15), which was estimated by a differential scanning calorimeter (Netzsch DSC 204 F1). In figure 1, differential scanning calorimeter (DSC) curves are shown, in which the peaks of primary crystallization for all three experimental alloys are marked by dashed lines. A kind of relaxation process starting at a temperature of about 500 K can also be detected in figure 1.

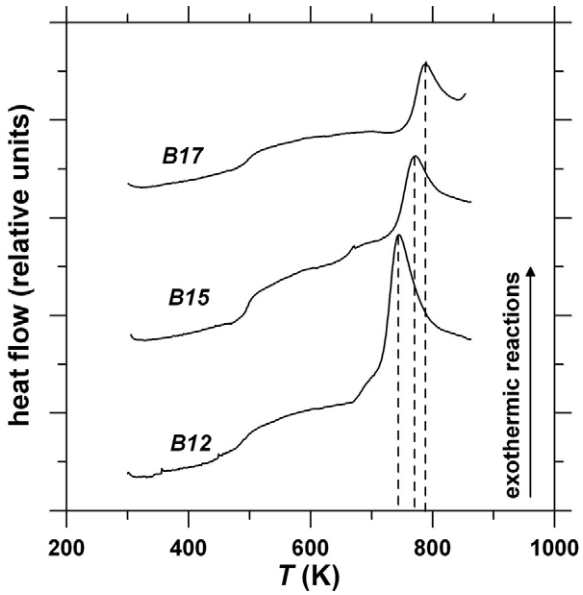

Figure 1. DSC crystallization curves obtained for the experimental alloys (10 K min^{-1}).

Table 1. Composition of experimental alloys prepared by the flow casting technique. The results of spectrometric analysis of flow-cast samples are in at.%.

Symbol for the alloy used in the text	Nominal composition	Fe	Mo	Cu	B
B12	$Fe_{79}Mo_8Cu_1B_{12}$	78.63	8.09	0.82	12.46
B15	$Fe_{76}Mo_8Cu_1B_{15}$	76.11	8.16	0.73	15.00
B17	$Fe_{74}Mo_8Cu_1B_{17}$	74.65	8.02	0.54	16.79

Table 2. Thermal pretreatment—qualitative characteristic of the resulting structure.

Symbol	T (K)/t (h)	Characteristic of the alloy microstructure
$t1$	683/1, 695/1, 695/5[a]	Very fine crystallites (size ∼3 nm) in relaxed matrix; very low number of large grains (size ∼1 μm)
$t2$	743/1	As $t1$ + low number of large crystallites (size ∼1 μm)
$t3$	773/1	As $t2$; greater number of large crystallites in colonies
$t4$	773/8	As $t3$; large crystallites often covered by a monolayer of smaller (∼50 nm) crystallites
$t5$	Thermal shock[b]	Crystals of α-Fe (size ∼100 μm) + Mo-rich borides (size ∼50 nm) + areas of relaxed matrix as sub-$t1$ (size ∼100 μm)

[a] All the anneals led to the same structure as indicated.
[b] 10 s exposure to the heat source in vacuum 3×10^{-6} mbar. The temperature of the source was kept at $T \cong 1273$ K, its effective area was about 3 cm^2 and the distance between the source and samples was 3 cm.

2.2. Structure of samples

In the as-received state, all alloys were amorphous with the exception of a surface layer (thickness about 300 nm), where about 6% of α-Fe was detected by conversion electron Mössbauer spectroscopy (similar to that in [14]). The presence of fine crystallites (size

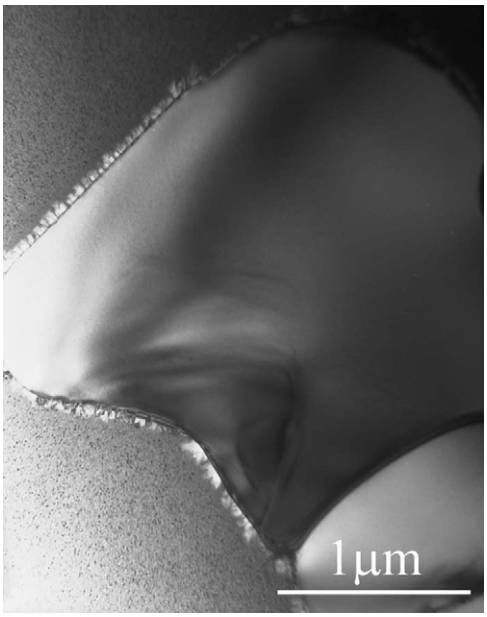

Figure 2. Example of the structure after $t4$ (TEM; alloy B15). Magnification 22 000×.

∼3–10 nm) in the surface layer was also confirmed by transmission electron microscopy (TEM). The samples for TEM were thinned electrolytically in a mixture of 95% CH_3COOH, 5% $HClO_4$; 95 V/14 °C and finished 5 min/3 kV/tilt 3.5° by precision ion polishing system GATAN 691.

In materials after $t1$–$t4$, three structure components were indicated, as is summarized in table 2: (i) individual fine crystals with size of about 3 nm in (ii) relaxed amorphous matrix, (iii) much greater crystals with typical size of about 1 μm, and (iv) thin (thickness ∼50 nm) monolayer of compact crystallites covering the large growing grains. All the components can be found in figure 2.

By the treatment $t5$, a fine-grained structure was prepared, consisting of three distinct components (figure 3): (i) an iron-rich crystalline phase C, (ii) the relaxed amorphous phase RA with fine α-Fe dispersion in it, and (iii) molybdenum-rich boride phase B.

An attempt was made to identify the alloy components by x-ray diffraction (XRD) using an X'Pert PRO instrument with Co Kα radiation: it can be seen in the lower part of figure 4 that the crystalline phase is formed prevailingly by α-Fe (bcc) (compare with the upper part of figure 4 obtained with slightly only relaxed B15 alloy). Moreover, certain portion of γ-Fe (fcc) can be also detected in the alloy after $t5$. The other peaks are due to boride phase. With respect to the typical ratio r = at.% Mo/at.% Fe = 0.83 obtained for phase B, it can be deduced that—on average—Mo prevails over Fe in the boride phase. An assessment of the particle size from the mean coherence length (MCL) was made with the help of the Rietveld analysis that is provided within the SW package X'Pert HighScorePlus (PANanalytical®) and using the JCPDS PDF-4 database. The assessment led to values MCL = (29 ± 2) nm for the boride phase (this agrees with the mean size of phase B in figure 3) and MCL = (15 ± 2) nm for α-Fe, which is reasonably close to the size of finely dispersed Fe particles in phase RA.

Despite the fact that alloys after $t5$ are not in thermodynamic equilibrium, the identity of boride phase B (figure 3) can be estimated by numerical assessment of the equilibrium diagram.

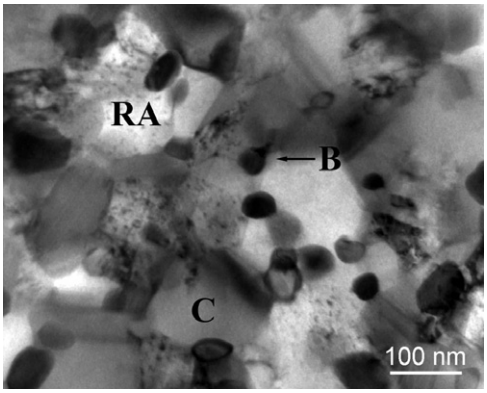

Figure 3. TEM micrograph of B15. C (crystallites): ratio r = at.% Mo/at.% Fe = 0.02 (mean grain size $d \sim 150$ nm), RA (relaxed amorphous with fine dispersion of α-Fe): $r = 0.09$ ($d \sim 150$ nm) and B (boride phase): $r = 0.83$ ($d \sim 30$ nm).

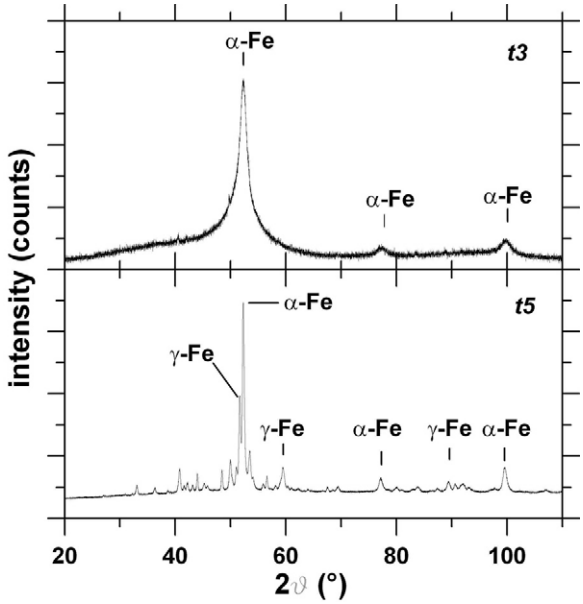

Figure 4. XRD spectrum measured with B15 alloy after relaxation $t3$ (upper part) and after the treatment $t5$ (lower part).

The result of the Thermo-Calc calculation is shown in figure 5. It can be seen that there are two borides M_3B_2 and M_2B in the equilibrium state that could be considered. Since the calculated Mo concentration in the latter one is very low (about 1 at.%), it can be deduced that B is, most likely, identical with the tetragonal M_3B_2 phase. This is a very stable boride present even in the melt, and it can be expected that it is preferred during the devitrification.

2.3. Diffusion measurements

The diffusion measurement was carried out by the serial sectioning technique with the radiotracers ^{59}Fe and ^{99}Mo. Thin radioactive layers of ^{99}Mo on the sample surfaces were

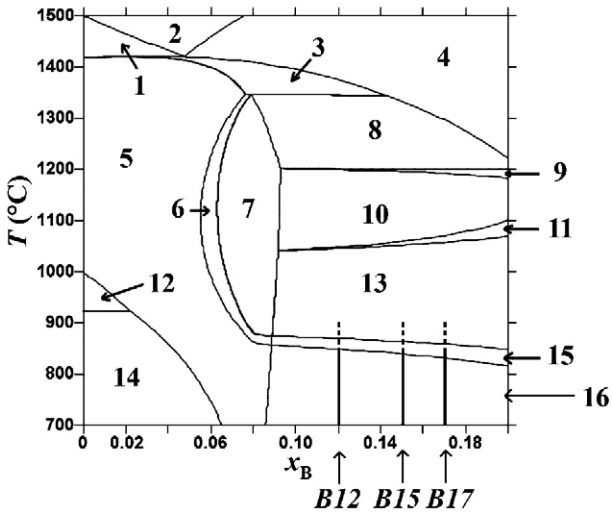

Figure 5. The section 8 at.% Mo, 1 at.% Cu of the quaternary alloy system FeMoCuB. Assessed by Thermo-Calc. Verticals B12, B15, B17 show schematically the treatment *t*5. 1—L + bcc, 2—L, 3—L + bcc + M_3B_2, 4—L + M_3B_2, 5—bcc + M_3B_2, 6—fcc + bcc + M_3B_2, 7—fcc + M_3B_2, 8—L + fcc + M_3B_2, 9—L + fcc + M_3B_2 + M_3B, 10—fcc + M_3B_2 + M_3B, 11—fcc + M_3B_2 + M_3B + M_2B, 12—bcc + M_3B_2 + μ, 13—fcc + M_3B_2 + M_2B, 14—bcc + M_3B_2 + μ, 15—bcc + fcc + M_3B_2 + M_2B, 16—bcc + M_3B_2 + M_2B.

deposited either by a direct dripping-and-drying technique or, alternatively, by vacuum evaporation. ^{99}Mo was used in the form of a 0.01 M solution of ammonium molybdate in NH_4OH. Layers of ^{59}Fe were electrodeposited from a diluted water solution of $^{59}FeCl_3$ in 0.5 M HCl (1:500) under conditions 30 V/5 mA cm^{-2}/10 min.

The samples were encapsulated in a Ta envelope and sealed in silica ampoules filled with pure (6 N) Ar. The diffusion anneals were carried out in a horizontal tube furnace in the temperature range 548–773 K (for times and temperatures, see tables 3 and 4). The temperature was registered by a Pt/Pt10Rh thermocouple and stabilized within $\pm$1 K.

The penetration profiles were obtained by the serial sectioning method using ion-beam sputtering with Ar^+ ions. The energy of the Ar^+ ions was 2 keV and the current density was kept constant at 1.9 mA cm^{-2}. Each sample was mounted on the rotating holder; the angle between the incident Ar^+ beam and the normal to the sample surface was 60°. This arrangement minimized the effect of cascade mixing and selective sputtering [5, 7].

A constant portion of sputtered-off material was collected continuously onto a moving thin polyester foil. After sputtering, the foil was slit in equal-sized cuts that were placed in plastic vials, together with the scintillation cocktail Filter Count, and their relative radioactivity was counted by a liquid scintillation counter (TRI-CARB 3170 TR/LS). Since no chemicals were added to the cocktail and the measurement was made after the tempering of all vials in the apparatus, no quenching effects influenced the results. The measured relative activity of the vial was proportional to the average concentration c of diffusant in the respective layer. The depth coordinate $x(\tau) = \tau/\tau_{\text{tot}}\ (1 - m_0/m)h$ at the sputter time τ was obtained from the mass of the sample before and after the sputtering (m_0 and m, respectively), from the total sputtering time τ_{tot} and from the thickness of the sample h after the sputtering.

Table 3. Diffusion coefficients D_v (in 10^{-20} m^2 s^{-1}) measured in alloy B15. The typical error in D_v is about 25%.

Segment[a]	Diffusant	Pretreatment	T (K)	t (s)	D_v (m^2 s^{-1})	Remark[b]
I	^{99}Mo	$t1$	649	5 400	0.952	Centre
				18 000	0.326	
			631	54 000	0.0807	
					0.0451	
			628	54 300	0.237	
			608	86 400	0.0450	
			588	259 200	0.0243	
	^{59}Fe	$t4$	673	7 200	1.79	Air
					3.08	Dull
		$t1$	649	5 400	0.294	Centre
		$t2$			0.332	
		$t1$	647	21 600	0.626	
		$t2$	630	54 600	0.121	
		$t1$		11 040	0.0985	
		$t2$			0.102	
II	^{99}Mo	$t1$	628	54 300	67.0	Centre
			608	86 400	21.2	
			588	259 200	8.40	
			568	324 420	1.86	
			548	604 800	1.02	
		$t2$	628	54 300	307	
			608	86 400	54.3	
			588	259 200	69.0	
			568	324 420	31.6	
			548	604 800	3.36	
	^{59}Fe	$t4$	673	7 200	23.3	Air
					28.0	Dull

[a] I—the near-surface steep part of the penetration profile, II—the 'tail' of the penetration profile.
[b] Air—measured at the air side of the ribbon, Dull—measured at the dull side and Centre—measured at the centre of the ribbon (after the removal of the surface layer some 2 μm thick).

3. Results and discussion

3.1. Penetration profiles

The primary results obtained in the present work are the penetration profiles, i.e., the dependences of the concentration of the diffusing nuclide (^{59}Fe or ^{99}Mo), c, on the penetration depth x below the original surface ($x = 0$) after a diffusion anneal of duration t. Examples of measured profiles can be seen in figures 6–8. Since the diffusion characteristics are evaluated from the slopes of $c(x, t)$, relative only concentrations in arbitrary units are plotted. It was proved in a couple of preliminary experiments (using the same diffusion temperature T and varied diffusion times t) that the measured curves are reasonably parallel after rescaling (near-surface parts in coordinates $\log c$ versus $x/t^{0.5}$, the tails either in coordinates $\log c$ versus $x/t^{0.258}$ or in coordinates $\log c$ versus $x/t^{0.45}$). This means that the distribution of concentration given by the curves is generated by diffusion.

3.2. Reconstruction of true concentration profiles

It is well known that both sputter depth profile analysis of fine multilayered structures and analysis of the very close vicinity (in order of an interatomic distance) of interfaces are

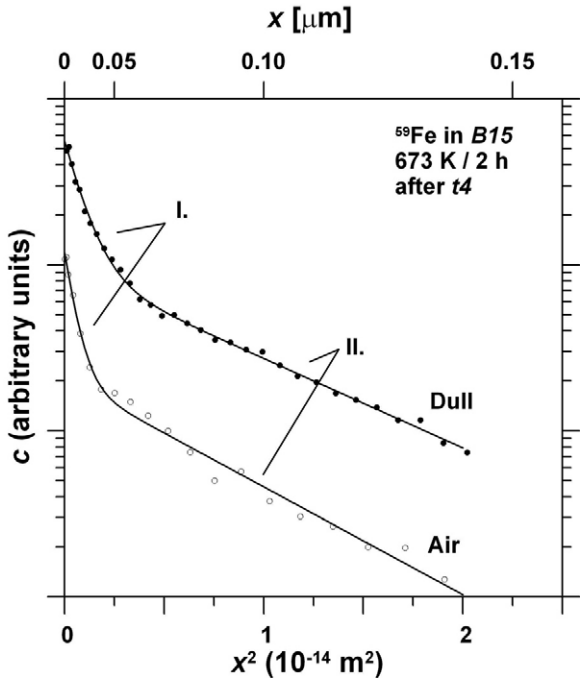

Figure 6. An example of a near-surface part of penetration profiles plotted in coordinates log c versus x^2.

Table 4. Values of sD_b (in 10^{-15} m^2 s^{-1}) for ^{59}Fe diffusion at $T = 673$ K, calculated with $\delta = 5 \times 10^{-10}$ m, $t = 7200$ s and $D_v = 2.44 \times 10^{-20}$ m^2 s^{-1}. For remarks on Air and Dull see table 3. The typical error in sD_b is about 50%.

Alloy	Pretreatment	sD_b	β	Remark
B12	*t*3	1.40	1080	Air
		1.76	1360	Dull
	*t*4	5.47	4240	Air
		7.34	5690	Dull
	*t*5	16.4		Air
B15	*t*3	3.00	2320	Air
		2.63	2040	Dull
	*t*4	5.03	3900	Air
		9.08	7040	Dull
	*t*5	13.0		Air
B17	*t*3	1.13	873	Air
		1.05	812	Dull
	*t*4	3.20	2430	Air
		4.56	3530	Dull
	*t*5	13.6		Air

influenced by several factors that limit the information on the true concentration distribution. They originate in the sputtering-induced changes of the sputtered surface and were discussed in detail, for example, in [5]. In general, the relation between the measured concentration profile

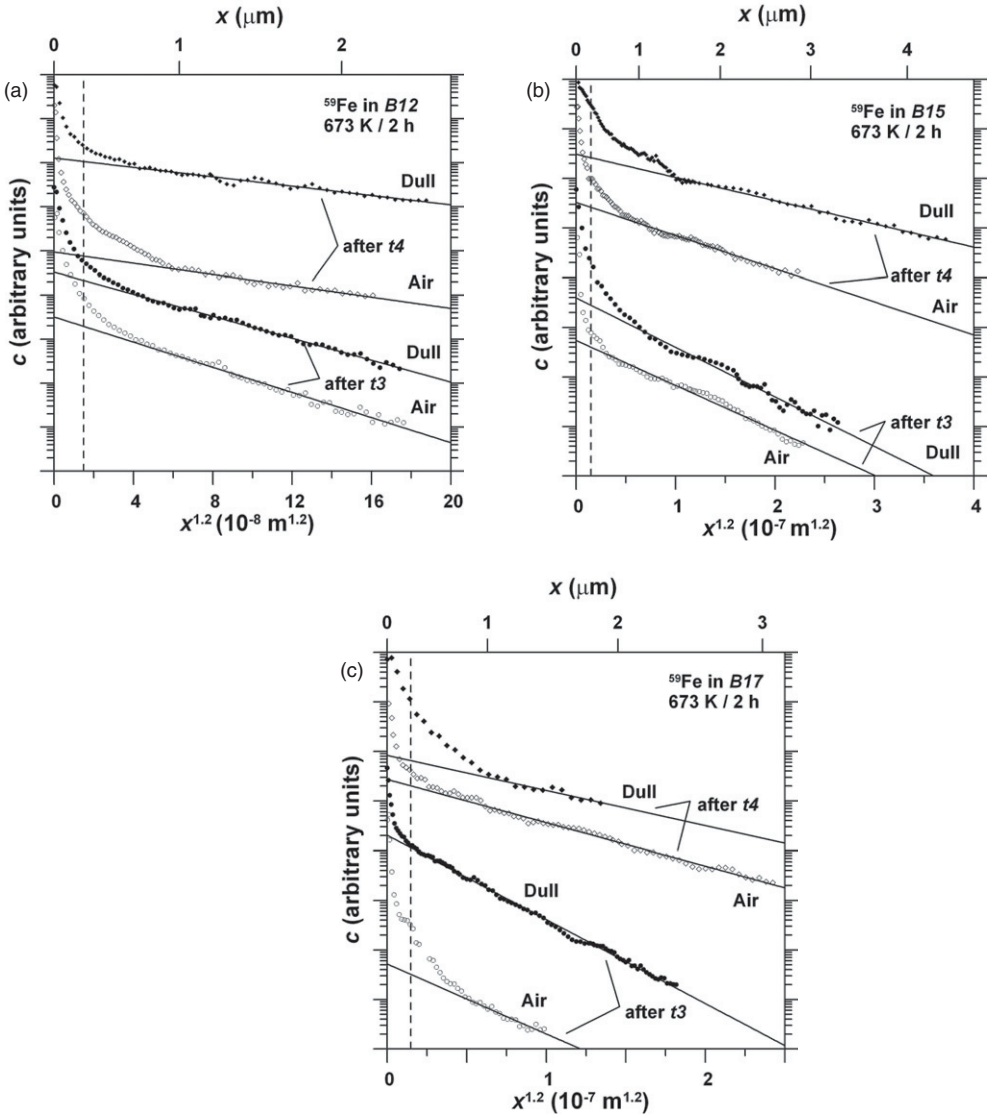

Figure 7. Penetration profiles measured after $t3$ and $t4$ in B12 (a), B15 (b) and B17 (c).

$c_{\mathrm{M}}(x,t)$ on the one hand and the 'true' profile $c(x,t)$ on the other is given by the convolution

$$c_{\mathrm{M}}(x,t) = \int_0^x c(\xi,t)\, f(x-\xi)\, \mathrm{d}\xi, \tag{1}$$

where f is the depth resolution function (DRF). It accounts for the influence of composition in the depth ξ upon the measured concentration in the depth $x > \xi$. Hence, the true profile can be obtained by the deconvolution of measured $c_{\mathrm{M}}(x,t)$, which is of course possible if the DRF is a known function. According to arrangement of the present experiment, it can be expected that the main effect upon the measured concentration profile comes from the cascade mixing. In such a case, the DRF can be written as an exponential [5, 15]:

$$f(x) \approx \exp\left(-\frac{x}{\lambda}\right), \tag{2}$$

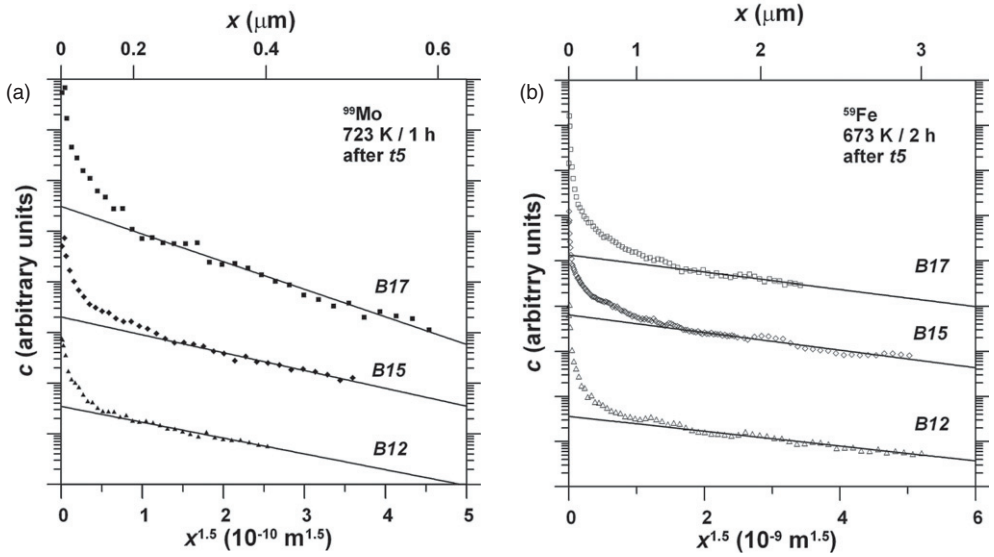

Figure 8. Diffusion of ^{99}Mo (a) and ^{59}Fe (b) in materials after $t5$.

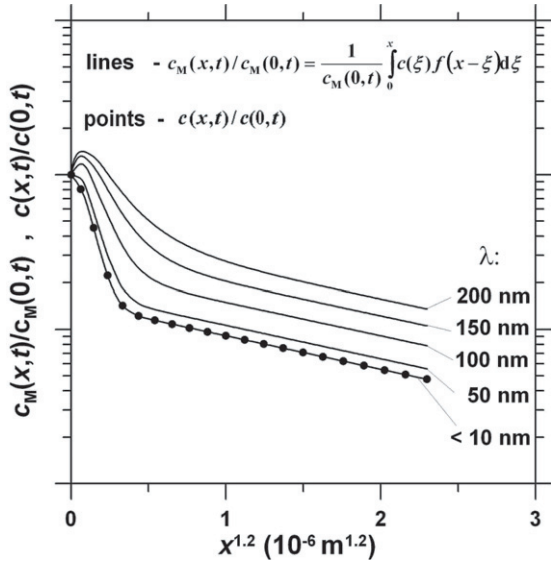

Figure 9. Calculated penetration profile—points; measured profile calculated numerically from equations (1) and (2)—lines.

where λ is a typical length characterizing the effect of cascade mixing. In figure 9, a comparison of c and c_M is shown. Profile c without convolution (points) is calculated for volume diffusion coefficient $D_v = 1\times10^{-19}$ m^2 s^{-1}, grain boundary diffusion coefficient $D_b = 5\times10^{-15}$ m^2 s^{-1}, grain boundary width $\delta = 5\times10^{-10}$ m, time $t = 8$ h and grain size $d = 10$ nm [16]. These numerical constants were chosen in order to simulate a typical measurement done in the present work. Lines in the figure show the convolution obtained numerically from equations (1) and (2) using the profile c calculated above without the convolution. It can be seen that c_M approaches

c for $\lambda < 10$ nm, which means that the deconvolution may not be done in the present work. Let us just mention that typical values of λ are of the order of nanometres [5].

It is worth noting that experimental assessment of the DRF in tracer experiment is extremely difficult. The response $f(x)$ to the 'pulse-shaped' concentration at the surface, $c(x, t) \sim \delta(0)$ ($\delta(0)$ is the Dirac delta function), is always spoiled by the uneven distribution of diffusant at the surface. Consequently, the DRF obtained experimentally is always too broad and, after the deconvolution, it produces unrealistically low diffusion coefficients.

3.3. Evaluation of diffusion characteristics

3.3.1. Initial part of the diffusion profile. It is illustrated in figure 6 that measured penetration profiles consist of a steep near-surface segment (marked as I) followed by a deeper part (II). If not too many points are available that span over not more than two orders of magnitude in c, the penetration profile can be well resolved into two Gaussian contributions, each of them describing its own independent mechanism of volume diffusion [7]. Hence, the profile can be well fitted by a combination of two terms (see the lines in figure 6):

$$c(x, t) = A \exp\left(-\frac{x^2}{4D_{\mathrm{v}}^{\mathrm{I}} t}\right) + B \exp\left(-\frac{x^2}{4D_{\mathrm{v}}^{\mathrm{II}} t}\right). \tag{3}$$

The diffusion coefficients $D_{\mathrm{v}}^{\mathrm{I}}$, $D_{\mathrm{v}}^{\mathrm{II}}$ in segments I and II, respectively, as well as constants A and B can be found as fitting parameters.

The measurement of penetration profiles was done both from the 'air' and from the 'dull' side of the ribbons. In order to avoid the influence of the partly crystallized layer (thickness some 300 nm) upon the values of D_{v}, measurement was performed also in 'central' part of ribbons (Centre) after grinding off a surface layer (about 2 μm thick). Obtained values of diffusion coefficients D_{v} are given in table 3.

It can be seen in figure 10 and table 3 that the values of $D_{\mathrm{v}}^{\mathrm{I}}$ do not depend significantly on the type of pretreatment, nor on the location of the diffusion zone (Air, Dull or Centre) and, at the same time, they are almost identical for Fe and Mo diffusion. It is also obvious from figure 10 that they are very close to Fe diffusion coefficients $D_{\mathrm{v}}^{\mathrm{I}}$ in similar NANOPERM-type alloys reported in the literature [7, 17–19]. Therefore, the obtained values of $D_{\mathrm{v}}^{\mathrm{I}}$ can be understood as reliable diffusion coefficients characterizing the Fe diffusivity in relaxed NANOPERM-type alloys.

3.3.2. Concentration tail of the penetration profile. The interpretation of concentration tails is much more difficult. There are some data reported in the literature [7] that ascribe the tails to a specific kind of fast volume diffusion. In figure 10 it can be seen, however, that the present values of $D_{\mathrm{v}}^{\mathrm{II}}$ for ^{99}Mo diffusion depend on the thermal pretreatment. Such a feature can lead to a conclusion that the concentration tail may characterize diffusion in a transition structure state and the results should be related only to an actual structural state of the alloy.

It was proposed in [7] that the fast-diffusion component (segment II) is due to the diffusion in a thin amorphous layer of intergranular phase (for values of $D_{\mathrm{v}}^{\mathrm{II}}$ reported in [7] measured for Fe diffusion in $Fe_{90}Zr_7B_3$—see line 5 in figure 10). The relative fractions of phases present in the relaxed FeMoCuB alloys reported in the Mössbauer study in [20] enable one to estimate that the thickness of the intergranular phase in NANOPERM-type alloys should not exceed several interatomic distances. Hence, such a situation resembles more the diffusion along 2D short-circuit paths than that in the 3D matrix. Therefore, an attempt was made in the present study to measure the profiles carefully down to a greater depth x and evaluate them in a way similar to that derived for the grain boundary diffusion (GBD) [16].

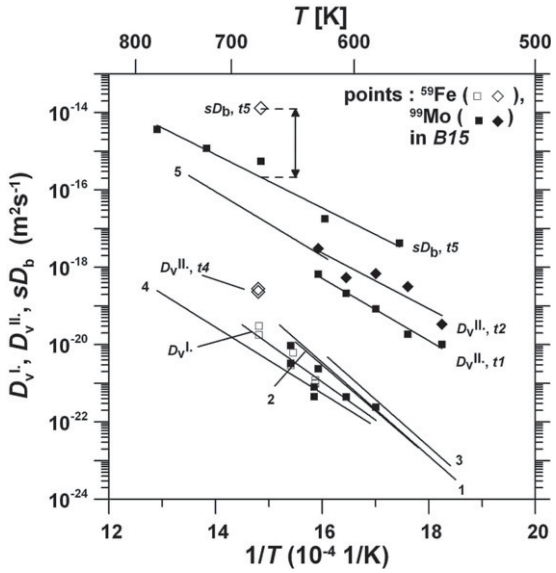

Figure 10. Arrhenius diagram of measured values of D_v^I, D_v^{II} and sD_b in B15 (points). Comparison with literature (D_v^I: line 1—Fe in $Fe_{80}B_{20}$ [17], 2—Fe in $Fe_{40}Ni_{40}B_{20}$ [18]. 3—Fe in $Fe_{68}Co_{17}B_{15}$ [19], 4—Fe in $Fe_{90}Zr_7B_3$ [7], D_v^{II}: 5—Fe in $Fe_{90}Zr_7B_3$ [7]). Arrow—difference between Fe and Mo grain boundary diffusion.

In figure 7, it can be seen that the concentration profiles measured for ^{59}Fe diffusion span over 3–4 orders of magnitude in c and even reach a depth of several μm. Dashed verticals in figures 7 indicate the surface layer that was partly crystallized even in the as-received state. Sufficient number of experimental points obtained for each profile enabled us to conclude that—after the pretreatments $t3$, $t4$—the tails are well linear in coordinates log c versus $x^{1.2}$, which is typical for B-type GBD kinetics [16]. Therefore, Le Claire's analysis [16] was applied to calculate values of the product sD_b (s and D_b are the segregation factor and diffusion coefficient of Fe in interfaces) that are listed in table 4. For the thickness of the interphase boundary, a value $\delta = 5 \times 10^{-10}$ m was taken. It is obvious from table 4 that the leakage parameter $\beta = \delta s D_b/(2D_v\sqrt{D_v t})$ is well above unity, and it is also easy to show that the mean diffusion length $2\sqrt{D_v t}$ is much smaller than the typical size of crystallites. These are conditions for type-B diffusion kinetics [16].

It was found (figure 11) that the calculated products sD_b do not depend significantly either on the side of the ribbon (the same results found for air and dull sides) or on the ratio Fe/B in the alloy. On the other hand, they systematically increase with the intensity of thermal pretreatment. We suggest a following explanation based on observed structure of treated samples (table 2). The dependence of D_v^{II} (figure 10) and interphase diffusivity sD_b (figure 11) on the type of pretreatment may be due to the effective thickness and type of interface between the growing crystallites and relaxed amorphous matrix. After $t1$–$t3$, segment II gives information on the diffusion flux $J_{GB}^{A/C}$ along 'plain and smooth' boundaries of A/C-type (schematically shown in figure 12; the fraction of C/C-type boundaries is negligible). The higher values of sD_b observed after $t4$ (compared to values measured after $t1$–$t3$) can be explained by two factors: (i) due to the layer of fine grains (figure 2), there are effectively about three times more diffusion paths per unit surface area of crystallites, which acts as if the grain boundary width δ was greater; (ii) about 2/3 of the paths are of the type C/C (schematically

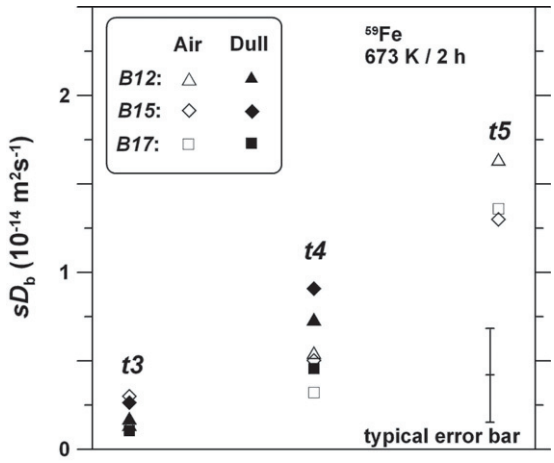

Figure 11. Comparison of diffusion characteristics of Fe along interphase boundaries in FeMoCuB alloys after pretreatments $t3$–$t5$. Air, Dull—Fe diffusion from the air and dull side, respectively.

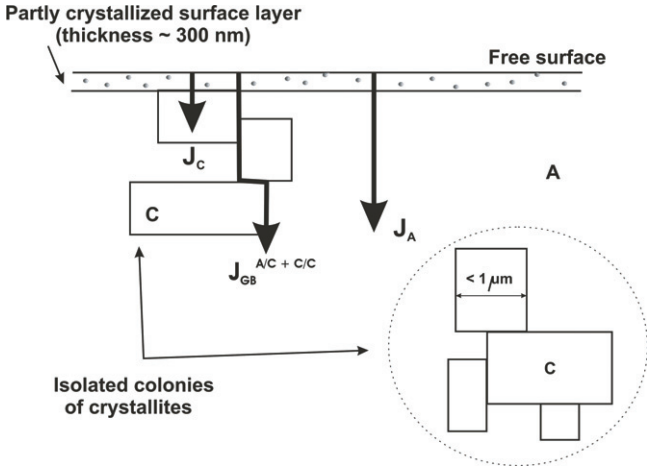

Figure 12. Structure of experimental alloys (schematically) after $t1$, $t2$ and $t3$ (cf real structure in figure 3). A—amorphous, C—crystalline, J_X—diffusion flux in X, $J_{GB}^{Y/Z}$—diffusion flux in GBs of type Y/Z.

shown in figure 13). Let us note just that it can be presumed that $J_{GB}^{A/C} \simeq J_{GB}^{RA/C} < J_{GB}^{C/C}$ because A/C-type and RA/C-type grain boundaries (GBs) are spatially more closed than C/C-type GBs.

To obtain diffusivities sD_b in the fastest C/C-type GBs, the diffusion was studied in shocked samples. After the treatment $t5$, these GBs are most frequent and they make the continuous diffusion paths (schematically shown in figure 14). Since the mean grain size is about 100 nm in this case, it may be expected that there is a transition regime between type-A and type-B GBD kinetics [21]. In this transition regime, the tails of penetration profiles are linear in coordinates log c versus $x^{1.5}$, which was observed in all cases (see the examples in

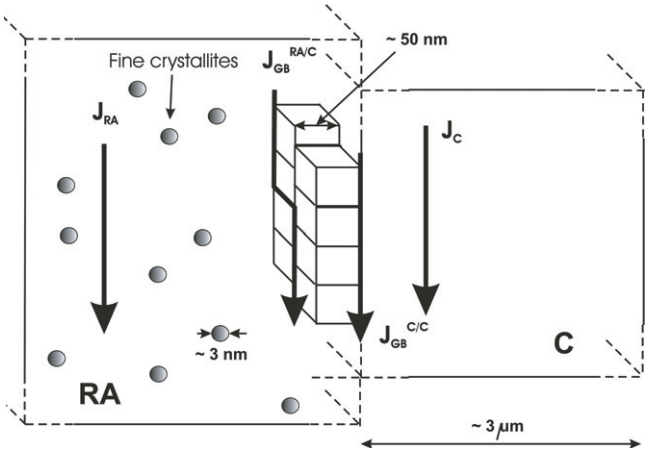

Figure 13. Structure of experimental alloys after *t*4—schematically (cf real structure in figure 2). RA—relaxed amorphous; other notation the same as in figure 12.

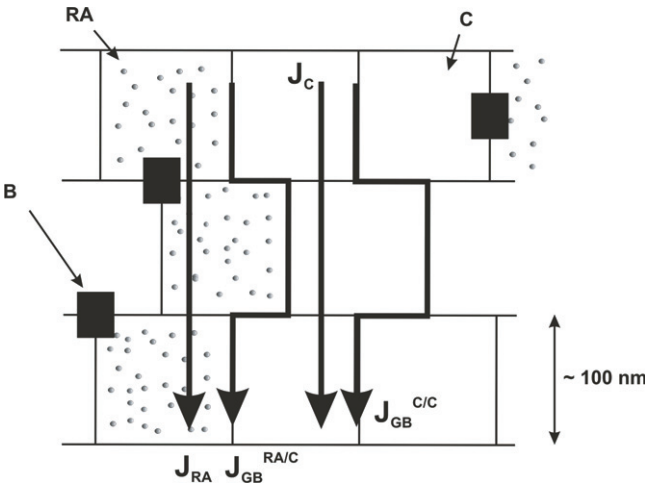

Figure 14. Structure of experimental alloys after *t*5—schematically (cf real structure in figure 3). B—boride particle. Other notation the same as in figures 12, 13.

figure 8). Values of diffusivities sD_b were calculated from the approximate relation

$$sD_b \cong 16.48 \frac{D^{0.1}}{\delta^{0.2} t^{0.9}} \left(-\frac{\partial \ln c}{\partial x^{1.5}} \right)^{-4/3}, \tag{4}$$

suggested in [21]. Results obtained for Fe at temperature $T = 673$ K are listed in table 4 and diffusivities of Mo in the temperature interval 573–773 K are summarized in table 5.

GB diffusivities sD_b of Fe and Mo at 673 K can be compared in figure 10. It can be seen that Fe diffuses by more than one order of magnitude faster than Mo in C/C GBs. This is caused, most likely, partly by the size factor and partly by the lower affinity of Fe to B in comparison with Mo.

Fitting of the Arrhenius equation $sD_b = (sD_b)_0 \exp(-Q/RT)$ has shown that the activation enthalpy Q (table 6) of Mo GBD increases with increasing concentration of B.

Table 5. Values of sD_b (in 10^{-17} m^2 s^{-1}) for ^{99}Mo diffusion, calculated from equation (4) [21] with $\delta = 5 \times 10^{-10}$ m and $D_v = 2.44 \times 10^{-20}$ m^2 s^{-1}. Pretreatment in all the cases: $t5$; segment: II. The typical error in sD_b is about 50%.

T (K)	t (s)	B12	B15	B17
773	1 800	283	369	135
723	3 600	109	115	54.2
673	3 600	33.1	55.3	14.8
623	86 400	5.60	1.8	1.4
573	864 000	0.650	0.420	0.0717

Table 6. Summary of Arrhenius parameters.

Diffusant	Alloy	Pre-treatment	Segment	sD_v^I or sD_b	$-\ln(sD_b)_0$ or $-\ln(sD_b^I)_0$ $(sD_b)_0$, $(sD_b^I)_0$ in m^2 s^{-1}	Q (kJ mol^{-1})	ΔT (K)
^{99}Mo	B12				15.78 ± 0.92	112.5 ± 5.1	
	B15	$t5$	II	sD_b	12.5 ± 2.8	132 ± 15	573–773
	B17				11.9 ± 2.1	140 ± 12	
^{99}Mo + ^{59}Fe	B15	$t1 + t2 + t4$	I	sD_v^I	12.0 ± 4.6	188 ± 24	588–673

This may be explained by trapping of Mo in the M_3B_2 phase at GBs (Mo is a majority M-component in the boride phase). It can be also seen in the table that values of Q for Mo GBD are significantly lower than the value of Q obtained for volume diffusion of Mo and Fe in a relaxed amorphous matrix.

4. Summary

It was concluded that the first segment of the concentration profile $c(x, t)$ should be attributed to bulk diffusion. The corresponding diffusion coefficient, D_v^I, does not depend significantly on the thermal treatment. The values of D_v^I both for Mo and Fe diffusion are close to one another, and agree quite well with the 'slow' diffusion component reported in the literature for Fe diffusion in similar NANOPERM-type alloys.

It seems likely that the second segment of $c(x, t)$ is more or less influenced by short-circuit diffusion along interfaces present in the alloy after the thermal pretreatment. It is difficult to compare results obtained with the two diffusants. The diffusion along interphase boundaries of A/C-type and RA/C-type is lower than that along the C/C grain boundaries. This may be explained by lower free volume in the former and higher free volume in the latter type of interface.

Mo-rich borides at grain boundaries act as traps for Mo diffusion—the increasing concentration of B in the alloy increases the activation enthalpy of Mo GBD.

Whereas values of D_v^I for Mo and Fe in $Fe_{91-y}Mo_8Cu_1B_y$ alloys are almost the same, a significant difference between the fast Fe and slow Mo GBD was observed in C/C-type grain boundaries: D_b for Fe $>$ D_b for Mo (it can be expected that s for Fe GBD $\cong$ 1 and s for Mo GBD > 1). This may be due partly to the size effect and partly to the lower affinity of Fe to B.

Since the growing crystalline phase contain minimum Mo in it, excess Mo must be driven in front of the crystallization front and redistributed to form borides. This occurs—partly at least—via Mo GBD. The slow Mo GBD may, in this way, contribute to structure stabilization of the studied alloys.

Acknowledgments

This work was supported by the Czech Science Foundation, project number 106/04/0228, and by IPM AS CR, project number AV0Z20410507. The authors would like express their thanks to Dipl. Eng. D Janičkovič for sample preparation, to Dr O Schneeweiss for XRD measurement, to Dr P Broz for Thermo-Calc calculation and to Dr M Svoboda for TEM measurements.

References

[1] Hasegawa R 2000 *J. Magn. Magn. Mater.* **215/216** 240
[2] Suzuki K 1999 *Mater. Sci. Forum* **312–314** 521
[3] Mehrer H and Dörner W 1989 *Defects Diffus. Forum* **66–69** 189
[4] Wenwer F, Gude A, Rummel G, Eggersmann M, Zumkley T, Stolwijk N and Mehrer H 1996 *Meas. Sci. Technol.* **7** 632
[5] Hofmann S 1998 *Rep. Prog. Phys.* **61** 827
[6] Lenser S, Daniel B S S, Zöllmer V, Erichsen J, Rätzke K, Deki S and Faupel F 2003 *Scr. Mater.* **48** 275
[7] Herth S, Eggersmann M, Eversheim P D and Würschum R 2004 *J. Appl. Phys.* **95** 5075
[8] Idzikowski B, Baszynski J, Škorvánek I, Müller K H and Eckert D 1998 *J. Magn. Magn. Mater.* **177–181** 941
[9] Miglierini M, Degmová J, Kaňuch T, Švec P, Illeková E and Janičkovič D 2005 *Properties and Applications of Nanostructured Alloys from Amorphous Precursors* ed B Idzikowski *et al* (Dordrecht: Kluwer–Academic) p 421
[10] Miglierini M, Degmová J, Kaňuch T, Švec P, Illeková E and Janičkovič D 2004 *Czech. J. Phys.* **54** D161
[11] Miglierini M, Seberíni M, Tóth I and Vitázek K 2003 *J. Magn. Magn. Mater.* **265** 243
[12] Illeková E, Janičkovič D, Miglierini M, Škorvánek I and Švec P 2006 *J. Magn. Magn. Mater.* **304** e636
[13] Illeková E 2005 *Properties and Applications of Nanostructured Alloys from Amorphous Precursors* ed B Idzikowski *et al* (Dordrecht: Kluwer–Academic) p 76
[14] Jirásková Y 2006 private communication—unpublished measurement
[15] Hofmann S 2001 *Thin Solid Films* **398/399** 336
[16] Kaur I, Mishin Y and Gust W 1995 *Fundamentals of Grain and Interphase Boundary Diffusion* (Chichester: Wiley)
[17] Horváth J, Ott J, Pfahler K and Ulfert W 1988 *Mater. Sci. Eng.* **97** 409
[18] Horváth J and Mehrer H 1986 *Cryst. Lattice Defects Amorphous Mater.* **13** 1
[19] Pavlovský J 1994 *Kov. Mater.* **32** 126
[20] Miglierini M and Greneche J M 2003 *J. Phys.: Condens. Matter* **15** 5637
[21] Divinski S V, Hisker F, Kang Y S, Lee J S and Herzig Chr 2003 *Interface Sci.* **11** 67